RSC Advances

PAPER

View Article Online
View Journal | View Issue

Open Access Article. Published on 04 November 2022. Downloaded on 11/2/2025 4:32:41 PM.
This article is licensed under a Creative Commons Attribution-NonCommercial 3.0 Unported Licence.

Check for updates

Cite this: *RSC Adv.*, 2022, **12**, 31650

A stable Fe/Co bimetallic modified biochar for ofloxacin removal from water: adsorption behavior and mechanisms†

Jiajie Hao,[a] Lieshan Wu,[a] *[a] Xiaowei Lu,[a] Yalin Zeng,[a] Bing Jia,[a] Tingting Luo,[a] Shixing He[a] and Liuling Liang[b]

In this study, Fe–Co-modified biochar (FMBC) loaded with iron (Fe) and cobalt (Co) bimetals after NaOH activation was prepared by pyrolysis using forestry waste cedar bark as a raw material to study its properties and the adsorption of ofloxacin (OFX). The surface structure and chemical properties were analyzed by BET, SEM-EDS, XRD, XPS, and FTIR characterization, and the results showed that the FMBC possessed a larger specific surface area and abundant surface functional groups. FMBC conformed to pseudo-second-order kinetic and Langmuir isotherm models, indicating that the OFX adsorption process on FMBC was a monolayer adsorption process and controlled by chemisorption. The saturation adsorption capacity of FMBC was 10 times higher than that of cedar bark biochar (BC). In addition, the effects of initial pH and coexisting ions on the adsorption process were investigated, and FMBC showed good adsorption, with the best adsorption capacity at pH = 7. Multiple adsorption mechanisms, including physical and chemical interactions, were involved in the adsorption of OFX by FMBC. TG, metal leaching, different water sources, and VSM tests showed that FMBC had good stability and was easily separated from water. Finally, the reusability performance of FMBC was investigated by various methods, and after five cycles it could still reach 75.78–89.31% of the adsorption capacity before recycling. Therefore, the FMBC synthesized in this study is a promising new adsorbent.

Received 25th August 2022
Accepted 24th October 2022

DOI: 10.1039/d2ra05334a

rsc.li/rsc-advances

1. Introduction

With the development of scientific technology, antibiotics were widely and heavily used in both medical and animal husbandry and aquaculture, leading to their frequent detection in the environment. Mainly, antibiotics enter the environment through four pathways: the process of antibiotic production, sewage, land application of municipal biosolids, and incorrect disposal of expired drugs.[1] Although their concentrations may be low in these environments, residual antibiotics could cause serious environmental and health problems due to cumulative effects, such as disruption of the human immune system, growth and escalation of antibiotic resistance genes, and damage to aquatic ecosystems.[2] The UK Antibiotic Crisis Survey analysis stated that approximately 700, thousand people worldwide died each year from drug-resistant bacterial infections and this number was expected to reach 10 million by 2050.[3]

Fluoroquinolone antibiotics, one of the most commonly used antibacterial drugs in the world, as the third largest sales of antibiotics, its global sales in 2009 reached 7.1 billion US dollars.[4] Ofloxacin (OFX) was one of the most heavily used fluoroquinolone antibiotics because it had a broad spectrum and high efficiency in treating infectious diseases in urinary and respiratory systems. It was reported that about 60–90% of OFX was not completely metabolized by the human body and was excreted through feces and urine,[5] and subsequently discharged into hospital or municipal wastewater, however, wastewater treatment plants could not completely remove it and the remaining OFX could reach surface water, groundwater and be deposited as biosolids.[6] Many studies in recent years had reported the presence of OFX in fresh water at concentrations ranging from 0.05 μg L^{-1} to 17.7 μg L^{-1},[7] and OFX was detected in the effluent of a hospital and a sewage treatment plant in France at an average daily amount of 3.7 g and 0.09 g, respectively.[8] Thus OFX also became one of the most frequently detected antibiotics in various water bodies (rivers, domestic sewage, and hospital wastewater).

To remove fluoroquinolone antibiotics from water, the main techniques available were adsorption,[9] oxidation,[10] photocatalysis,[11] and biodegradation.[12] Among them, adsorption had the advantages of simple operation, low cost, high efficiency, and environmental friendliness, and had great potential for

[a]Guangxi University, School of Resources Environment and Materials, Nanning, 530004, China. E-mail: wuls312@163.com

[b]Guangxi Zhuang Autonomous Region Ecological and Environmental Monitoring Centre, Nanning 530028, China

† Electronic supplementary information (ESI) available. See DOI: https://doi.org/10.1039/d2ra05334a

© 2022 The Author(s). Published by the Royal Society of Chemistry

Open Access Article. Published on 04 November 2022. Downloaded on 11/2/2025 4:32:41 PM.
This article is licensed under a Creative Commons Attribution-NonCommercial 3.0 Unported Licence.

large-scale applications.[13] Common adsorbent materials could be classified as activated carbon, graphene oxide, carbon nanomaterials, biochar, and clay minerals.[14–18] Among them, biochar was a solid material rich in carbon, obtained by thermochemical transformation of biomass under anaerobic/oxygen-limited conditions,[19] which was mainly applied for soil improvement, waste resource utilization, climate change mitigation, and energy production in environmental management, with good social and financial benefits.[20] The conversion of waste biomass into biochar had received increasing attention due to its potential for resource utilization and waste management. Biochar, a new low-cost adsorbent material, was well demonstrated in the scientific literature, possessing many reviews,[21,22] which had a large specific surface area, porous structure, rich surface functional groups, and mineral composition.[23]

The main biomass sources used for biochar were from agriculture (crops, herbaceous plants, and plantations), forestry (logging residues, wood processing by-products), and organic wastes (food industry). The International Renewable Energy Agency estimated that the global biomass supply potential would reach 147 EJ in the next 10 years, of which about 24–43 EJ would come from forestry, and the highest supply potential would amount to about 43–77 EJ per year in Asia and Europe.[24] From the perspective of sustainable development and comprehensive resource utilization, recycling forestry waste that was often discarded to decompose naturally or burned by factories could effectively reduce some of the environmental impacts caused by its combustion. Numerous studies conducted showed that bark was one of the most widely used adsorbent materials in studies of pollutant removal from water.[25] Bark, as a waste produced in large quantities from forest harvesting and wood processing, was estimated to total no less than 100 million m^3 per year in industrially developed countries worldwide, and a total of more than 3 million m^3 per year in China.[26] Currently, barks were mainly used as an energy source for direct combustion in sawmills and pulp mills, or as compost for horticultural usage,[27] while most of them were disposed of in the natural environment. In southern China, cedar trees were widely planted, while the abundant cedar bark resources had been neglected; therefore, the preparation of biochar from cedar bark could reduce its production cost and was of great practical significance to realize the resource utilization of forestry waste.

Since the adsorption capacity of biochar obtained by direct pyrolysis of biomass was low, it was often enhanced by physical and chemical modification of biochar to enrich the functional groups on its surface and increase its specific surface area and porosity. The addition of activation media (such as KOH, and NaOH) during pyrolysis could lead to higher porosity and the addition of metal salts could help to improve the properties of the prepared materials.[28,29] In addition, the rapid separation of biochar from water not only reduced the risk of releasing adsorbate after adsorption, but also solved the problem of difficult separation and recovery of powder adsorbent from solution during adsorption. Thus, biochar loaded with magnetic metal elements offered the possibility to achieve separation and recycling.[22]

As far as we know, there has not been a study to evaluate the adsorption of magnetic biochar prepared from cedar bark as biomass modified with Fe and Co bimetals for the removal of antibiotics from water. Therefore, in this study, Fe–Co-modified biochar (FMBC) was prepared by pyrolysis using low-cost cedar bark as raw material, which was further modified with iron (Fe) and cobalt (Co) bimetals after NaOH activation. The objectives of this study were to: (1) investigate the main adsorption mechanism of FMBC on OFX by characterization, kinetic, and isothermal analysis. (2) The effects of initial pH and coexisting ions on the adsorption capacity of FMBC were systematically investigated. (3) The stability and regeneration performance of FMBC were explored to evaluate its practical application.

2. Materials and methods

2.1 Materials

The cedar bark was collected from a wood processing plant (Guangxi Province, China); sodium hydroxide (purity ≥ 98.0%), ferric nitrate nonahydrate (purity ≥ 98.5%), and cobalt nitrate hexahydrate (purity ≥ 98.5%) were purchased from Guangdong Chemical Reagent Engineering Technology Research and Development Center (Guangdong Province, China), and OFX (purity = 98.0%) was purchased from Shanghai Maclean Biochemical Co. All chemicals in this study were of analytical purity grade, and deionized water (DI water) was used for all solutions.

2.2 Preparation of biochars and characterization

A schematic illustration of the preparation process of biochar was shown in Fig. S1.† Cedar bark biochar (BC), alkali modified biochar (MBC) and Fe–Co-modified biochar (FMBC) were all prepared by nitrogen pyrolysis, the typical preparation process and characterization details of samples were provided in the Text S1 and S2.†

2.3 Adsorption experiment

Unless otherwise stated, all adsorption experiments were performed by putting 0.05 g of biochar into a 500 mL OFX solution with a mass concentration of 20 mg L^{-1} in a 500 mL conical flask, shaking it for 12 h in a water bath thermostatic oscillator at 160 rpm and 25 °C. The pH of the OFX solution was adjusted to a range of 3 to 11 using 0.1 mol per L NaOH or HCl solution in the FMBC initial pH experiment. All experiments conducted in this study were carried out three times, and OFX solutions were filtered through 0.45 μm microporous filter membranes before measurement.

The detailed experimental methods of adsorption kinetics, isotherms, recycling experiment, and data analysis were summarized in Text S3 and S4.†

3. Results and discussion

3.1 Characterization of biochar

3.1.1 BET. As shown in Fig. 1, a further study was performed using N_2 adsorption/desorption analysis to measure the pore size distribution of the FMBC. According to the

Open Access Article. Published on 04 November 2022. Downloaded on 11/2/2025 4:32:41 PM.
This article is licensed under a Creative Commons Attribution-NonCommercial 3.0 Unported Licence.

International Union of Pure and Applied Chemistry (IUPAC) classification of adsorption isotherm-lag rings,[30] FMBC showed typical IV N_2 adsorption isotherm and H4-type hysteresis loop, which proved the existence of microporous and mesoporous structure. Based on the Brunauer–Emmett–Teller (BET) method, Table 1 showed that the calculated specific surface area of BC, MBC, and FMBC were 45.993, 416.859, and 496.423 $m^2\ g^{-1}$, respectively, with pore volumes of 0.051, 0.185, and 0.498 $cm^3\ g^{-1}$ and average pore diameters of 4.402, 3.951 and 4.012 nm, respectively. It was indicated that the specific surface area of FMBC after doping of Fe/Co increased nearly 11 times compared with that of BC before modification, and such a high specific surface area and the presence of micropores and mesoporous could provide a larger contact area for subsequent adsorption.

3.1.2 SEM-EDS. The surface morphology of BC, MBC, and FMBC was analyzed by scanning electron microscope (SEM) images. Fig. 2(a), (b) and (c) showed the SEM images of BC, MBC, and FMBC magnified at 10 K magnification, respectively. The BC surface (Fig. 2(a)) was flat and smooth without pores. However, the original smooth surface was destroyed after NaOH alkali modification, and the surface of MBC (Fig. 2(b)) was eroded to form a rough porous structure, the CO, CO_2, and other gases produced at high temperatures were lost through the pores, which resulted in the formation of micropores on the MBC surface.[31] Furthermore, the FMBC (Fig. 2(c)) showed a more irregular, uneven, and pore-developed surface morphology after loading with Fe/Co metals, and the number of micropores on the surface increased substantially. Moreover, the FMBC at 15 K of magnification (Fig. 2(d)) could clearly be observed to have many small particles attached to the surface, which may be the result of doping of Fe/Co metals formed by $CoFe_2O_4$ could provide more active sites for adsorption.[32] Also, micro-flowers stacked in blade-like structures were observed on the surface of FMBC (Fig. 2(e)), which were also Fe and Co conjugates,[33] due to the fact that the morphology of the products was highly dependent on the Fe/Co content ratio, showing different shapes.[34]

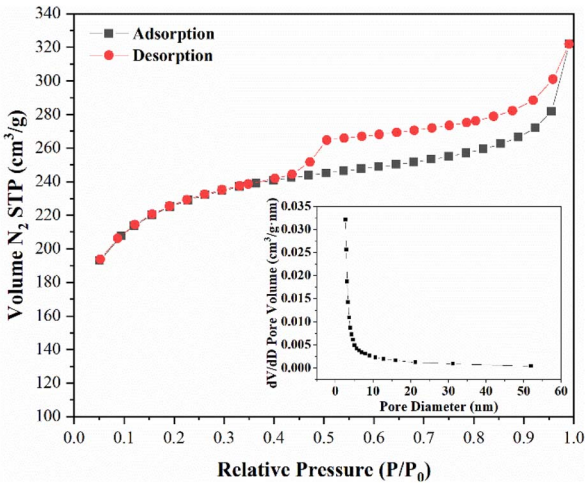

Fig. 1 N_2 adsorption–desorption isotherms and Barrette–Joyner–Halenda pore size.

Table 1 Physical properties of BC, MBC, and FMBC

Biochar	Surface area ($m^2\ g^{-1}$)	Pore volume ($cm^3\ g^{-1}$)	Pore diameter (nm)
BC	45.993	0.051	4.402
MBC	416.859	0.185	3.951
FMBC	496.423	0.498	4.012

EDS was used to examine the elemental composition of the materials, and Table S1† listed the elemental composition of BC, MBC, and FMBC. The main component of biochars was C. Before modification, BC had a high content of C thus forming a relatively flat carbon surface structure, which could be clearly seen in the SEM image. After NaOH alkali modification, the C content of MBC decreased from 95.83% to 88.04%, which was due to the loss of CO, CO_2 and other gases generated at high temperatures through the pores, resulting in the formation of more micropores on the surface of MBC and a lower carbon content. After doping of metals, the percentage of C content was further reduced due to the increase of O content and the presence of Fe and Co elements, so FMBC had the highest O/C ratio, indicating that the modified FMBC had more oxygen-containing functional groups.[35] From the EDS spectra of material FMBC in Fig. 3, it was clear that the main components of FMBC were C, O, Ca, Fe and Co, and Fe and Co elements were uniformly distributed on the surface of the material, indicating that the preparation of material FMBC was successful.

3.1.3 XRD. The X-ray power diffraction (XRD) patterns of all the samples were shown in Fig. 4(a). From the XRD spectra of BC and MBC, the (002) and (100) diffraction surfaces could be indicated at 2θ of about 23° and 43°,[36] which suggested the formation of amorphous carbon with amorphous carbon structure and graphitic structure, which contributed to the π–π electron donor–acceptor (EDA) interactions with the aromatic ring of OFX. The peaks of FMBC at $2\theta = 18.29°$, 30.08°, 35.44°, 43.06°, 53.44°, 56.97°, 62.58°, and 74.01° were characteristic peaks of (111), (220), (311), (400), (422), (511), (440) and (533) in $CoFe_2O_4$ [JCPDS: 22-1086],[37] and peaks at $2\theta = 44.72°$, 65.10°, and 82.42° were characteristic peaks of (110), (200) and (211) in Co_3Fe_7 [JCPDS: 48-1817].[38] These peaks of FMBC were stronger and sharper, manifesting the better crystallinity of $CoFe_2O_4$ and Co_3Fe_7 in FMBC. The XRD results showed that Fe and Co were successfully introduced into the FMBC, further confirming that the metallic small particles and micro-flowers present in the above SEM were the two elements Fe and Co in the form of metal oxides and alloys on the FMBC.

3.1.4 XPS. As shown in Fig. 4(b), the sharp peaks at 284.21, 531.40, 399.07, 711.00, and 782.10 eV in the full spectrum of FMBC could be ascribed to C 1s, O 1s, N 1s, Fe 2p, and Co 2p, accounting for 82.49%, 12.68%, 1.94%, 1.62%, and 9.31%, respectively. These results indicated that Fe and Co were successfully supported on FMBC surface after bimetallic activation. In addition, the full spectrum of FMBC-OFX showed that fluorine element (F 1s, 0.3%) peaks appeared, and nitrogen

 © 2022 The Author(s). Published by the Royal Society of Chemistry

Open Access Article. Published on 04 November 2022. Downloaded on 11/2/2025 4:32:41 PM.
This article is licensed under a Creative Commons Attribution-NonCommercial 3.0 Unported Licence.

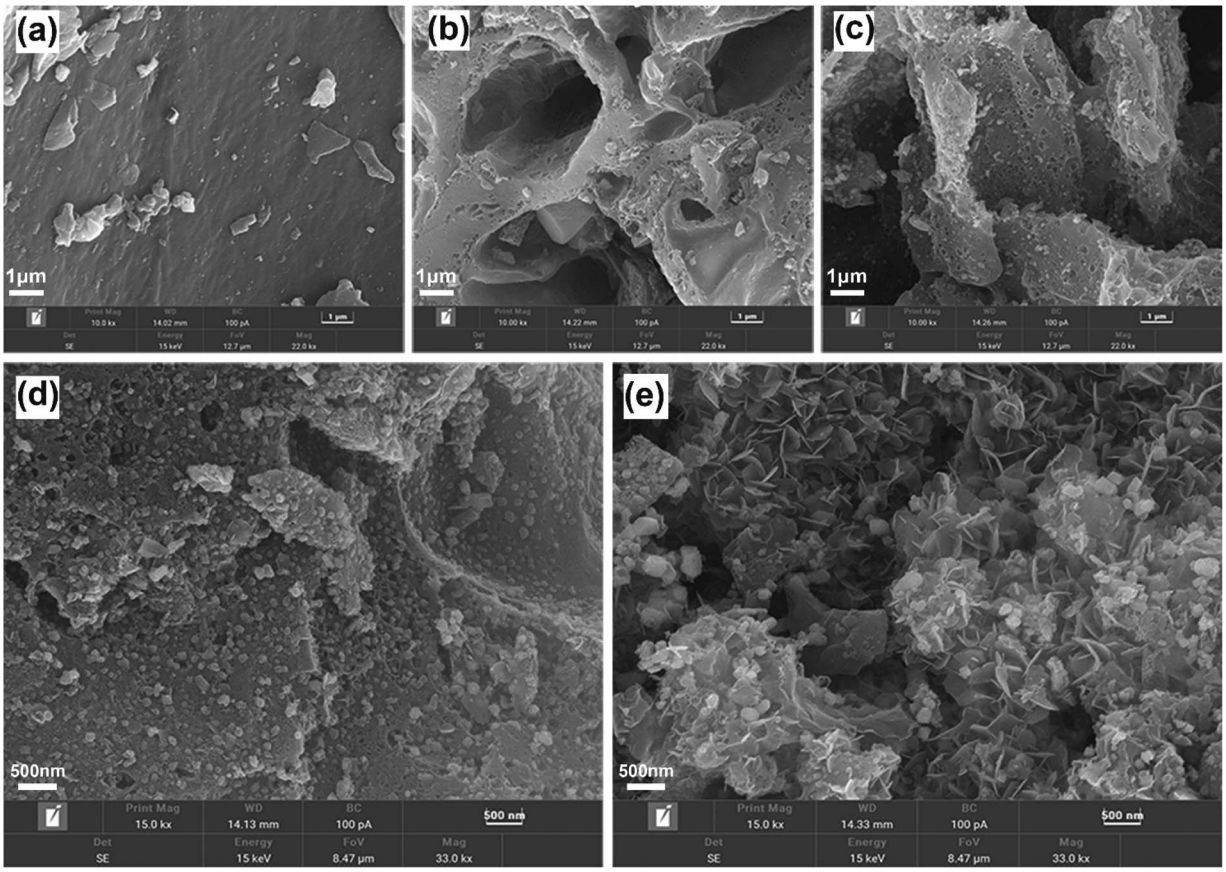

Fig. 2 SEM images of (a) BC, (b) MBC, (c) FMBC at 10 K of magnification, and (d and e) FMBC at 15 K of magnification.

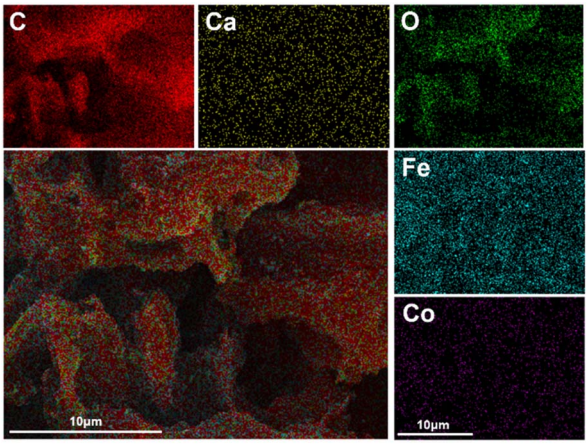

Fig. 3 EDS mapping images of FMBC.

element (N 1s, from 1.97% to 2.51%) peaks enhanced, which could be attributed to the adsorption of OFX containing fluorine and nitrogen on the surface of FMBC.

Fig. S2(a)–(d)† showed the C 1s and O 1s spectra of BC and FMBC, the peaks in the C 1s spectra corresponded to C–C/C=C, C–O, and O–C=O bonds.[37] The peaks in the O 1s spectra corresponded to C–O and C=O bonds, respectively. While the peak fitted at 530.27 eV in the FMBC corresponded to O–M bonds,[38] indicating that metal oxides were produced during the modification process, which was consistent with the presence of $CoFe_2O_4$ in the above SEM and XRD. Fig. S2(e) and (f)† showed the Fe 2p and Co 2p spectra of FMBC, respectively. The Fe 2p spectra showed peaks corresponded to Fe 2p3 and Fe 2p1, respectively, where the peaks at 711.45 eV and 724.25 eV were attributed to Fe^{2+}, the peaks at 714.87 eV and 727.67 eV were attributed to Fe^{3+}, the peaks at 719.23 eV and 733.03 eV were attributed to the satellite peaks of Fe^{3+}.[32,33] The Co 2p spectra showed peaks corresponded to Co 2p3 and Co 2p1, respectively, where the peaks at 781.37 eV and 796.06 eV were attributed to Co^{3+} and the peaks at 789.45 eV and 804.14 eV were attributed to the satellite peaks of Co^{2+}, the peaks at 786.14 eV and 800.83 eV peaks were attributed to Co^{2+}.[39] The X-ray photoelectron spectroscopy (XPS) results further confirmed that the FMBC surface had abundant functional groups, Fe and Co were present in it in various valence forms.

3.2 Adsorption kinetics

In this study, the obtained kinetic experimental data were fitted nonlinearly using the pseudo-first-order model, pseudo-second-order model, and intraparticle diffusion model. From Fig. S3(a) and (b),† it was seen that the adsorption amounts of BC, MBC, and FMBC increased rapidly within the initial 5, 10, and 30 min, then gradually slowed down, and reached the equilibrium

Open Access Article. Published on 04 November 2022. Downloaded on 11/2/2025 4:32:41 PM.
This article is licensed under a Creative Commons Attribution-NonCommercial 3.0 Unported Licence.

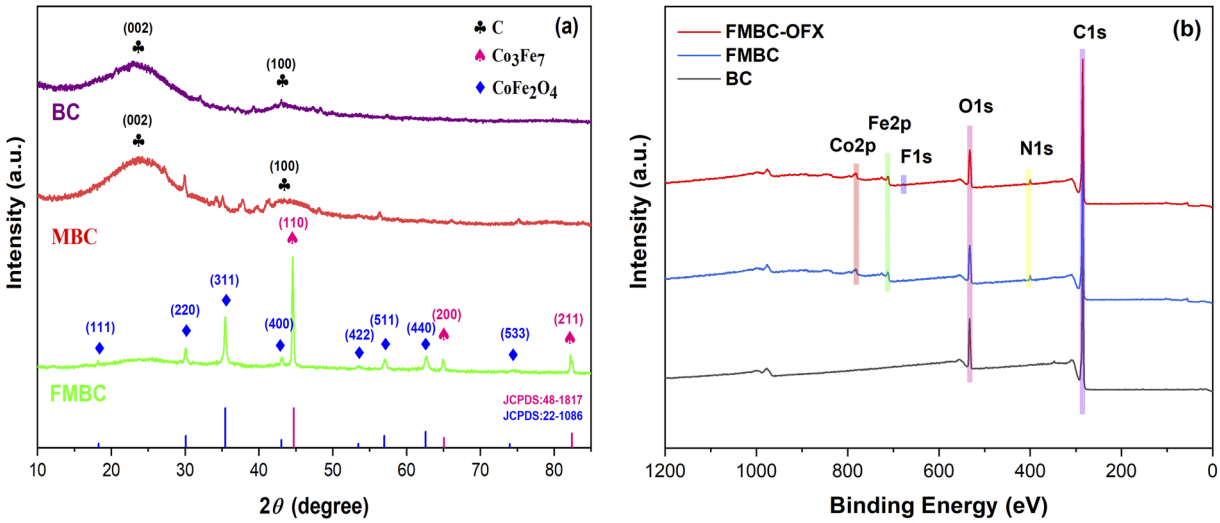

Fig. 4 (a) XRD patterns of BC, MBC, and FMBC; (b) XPS full spectra of BC and FMBC before and after adsorption of OFX.

basically at 20, 180, and 360 min, respectively. The equilibrium adsorption capacity of biochar for OFX was FMBC > MBC > BC. Both the alkali and metal modification improved the ability of BC to adsorb OFX, suggesting that surface oxygen-containing functional groups and small metal particles play an important role in the adsorption of OFX. As shown in Table 2, the pseudo-first-order model was more consistent with the process of OFX removal by BC ($R_1^2 = 0.9981 > R_2^2 = 0.8611$), indicating that the physical adsorption mechanism dominated the process of OFX adsorption on BC. While the pseudo-second-order model was more consistent with the process of OFX removal by MBC and FMBC ($R_2^2 = 0.9728$–$0.9781 > R_1^2 = 0.9008$–0.9539). Furthermore, the q_e values of 11.9012 and 60.2306 mg g^{-1} obtained from the pseudo-second-order model were closer to the experimental values of 12.3862 and 58.0110 mg g^{-1}. These results confirmed that the adsorption of OFX on MBC and FMBC was dominated by a chemisorption mechanism,[40] which was consistent with the kinetic behavior of adsorption reported by Yongfei Ma *et al.*[41]

To further identify the possible rate-limiting step and diffusion mechanisms of OFX adsorption onto BC, MBC and FMBC, thus intraparticle diffusion model was adopted to fit the experimental data, the fitted results were in Table S2.† However, it failed to demonstrate a good agreement with the experimental data since the non-linear regression coefficient (R^2) of BC was significantly lower compared to pseudo-first-order and pseudo-second-order models. Thus, intraparticle diffusion was unlikely to be the rate controlling step in the sorption of OFX onto BC. As shown in Fig. S3(c),† the adsorption process could be divided into three phases. The first stage was liquid film diffusion,[42] in which OFX molecules were transferred from the bulk solution toward the adsorbent surface. The diffusion rate constant ($K_1 = 2.7939$ mg (g min$^{1/2}$)$^{-1}$ of OFX adsorption onto FMBC was greater than those of MBC and BC ($K_1 = 1.9758$ mg (g min$^{1/2}$)$^{-1}$ and $K_1 = 0.2795$ mg (g min$^{1/2}$)$^{-1}$). It suggested that the liquid film diffusion on FMBC was more distinct which was due to its larger specific surface area than the two.[43] The second stage was intraparticle diffusion, where OFX molecules diffused from the outer surface to the inner structure of the adsorbent through the rich pores of MBC and FMBC, and then combined with the adsorption sites in mesopores and micropores. The third stage was equilibrium adsorption, which took a long time to reach and was mainly limited by the reduction of the available active sites on adsorbents. C value could be used to evaluate the diffusion resistance. The lower C_1 values described that weak liquid diffusion resistance in the initial stage due to the existence of large numbers of unoccupied active sites. After that, the active sites were occupied by OFX, and the migration of OFX was hindered, the larger C value indicated a greater diffusion resistance of OFX in mesopores and microporous relative to the diffusion resistance of liquid membranes. A higher C value illustrated a thicker boundary layer, which demonstrated the main control for OFX adsorption on FMBC was intraparticle diffusion.[44] Furthermore, a non-zero C value meant that the

Table 2 Parameters of pseudo-first-order model and pseudo-second-order model

	Pseudo-first-order model			Pseudo-second-order model		
Biochar	q_e (mg g^{-1})	k_1	R_1^2	q_e (mg g^{-1})	k_2 (g mg^{-1} min^{-1})	R_2^2
BC	3.1348	2.2419	0.9981	3.1509	2.9702	0.8611
MBC	11.1028	0.0662	0.9008	11.9012	0.0079	0.9728
FMBC	53.9685	0.0135	0.9539	60.2306	0.0003	0.9781

 © 2022 The Author(s). Published by the Royal Society of Chemistry

Open Access Article. Published on 04 November 2022. Downloaded on 11/2/2025 4:32:41 PM. This article is licensed under a Creative Commons Attribution-NonCommercial 3.0 Unported Licence.

curve did not pass through the origin, demonstrating that intraparticle diffusion was not the only rate-limiting step for adsorption and liquid film diffusion controlled the adsorption process simultaneously.[45]

3.3 Adsorption isotherms

In this study, the obtained experimental data were fitted non-linearly using Langmuir, Freundlich, and Temkin isotherms model (Fig. S3(d)–(f)†). Langmuir isotherms model was usually to estimate the theoretical maximum adsorption amounts of adsorbents, also it assumed that the adsorption process was monolayer chemisorption and adsorbates were homogeneously distributed on the surface of the adsorbent without horizontal/longitudinal interaction. Freundlich isotherms model described that the adsorption process was a multilayer that occurred on the heterogeneous surface of the adsorbent.[46] Temkin isotherm model assumed a uniform distribution of the binding energies and the adsorption free energy as a function of the surface coverage. This model mainly described the adsorption process as chemisorption through electrostatic interaction.[47]

The model parameters in Table S3† showed that BC and MBC were more consistent with the Freundlich model, and the adsorption of OFX was non-homogeneous multilayer adsorption. On the basis of its high correlation coefficient (R^2), the Langmuir model suited better the adsorptive mechanism of OFX on FMBC than the Freundlich and Temkin models, indicating that the adsorption behavior observed was largely monolayer adsorption. The K_F value in Freundlich represented the strength of the interaction between the adsorbent and the adsorbate, the larger the K_F value, the greater the affinity,[48] and the order in Table S3† was FMBC > MBC > BC, indicating that FMBC had the highest affinity for OFX. $1/n$ value was related to the ease of adsorption reaction, all $1/n$ values were between 0 and 1, further confirming that the adsorption was favorable.[49] In this study, the Temkin model for FMBC was also well fitted owing to excellent ($R^2 = 0.9085$), indicating electrostatic interaction to be significantly responsible for the adsorption mechanism of OFX using FMBC.[47] The b_T values of MBC and FMBC (4.9763 and 13.8008 kJ mol^{-1}) were higher than 4.2 kJ mol^{-1}, demonstrating that chemical adsorption was the key process in the adsorption of OFX on biochars and therefore might have an existence of endothermic adsorption,[2] which was consistent with the results of the kinetic analysis described above. According to the Langmuir model, the saturation adsorption capacity (q_m) of FMBC was 142.1914 mg g^{-1} for OFX, which was about 5 and 10 times higher than those of MBC (26.4475 mg g^{-1}) and BC (14.2864 mg g^{-1}), respectively. Studies had shown that the doping of Fe and Co acted synergistically to improve the adsorption capacity of the material.[50] Therefore, in this study, Fe/Co doping further enhanced the adsorption capacity of FMBC for OFX on the basis of alkali modification.

3.4 Adsorption process influencing factors

3.4.1 Effect of initial pH. Solution pH was a crucial environmental factor that affected the surface charge of the adsorbent and the form of adsorbent ions present in water. Fig. 5(a) showed that the adsorption of OFX by FMBC varied with the pH of the solution. FMBC reached the maximum adsorption capacity at pH = 7, with 160.24 mg g^{-1}. An aqueous solution of OFX existed in three ionic states because of two pK_a values (pK_{a1} = 6.10 and pK_{a2} = 8.28).[51] It could be seen that OFX mainly existed in the form of cations (OFX^+) when pH < pK_{a1}; when pH > pK_{a2}, it mainly existed in the form of anions (OFX^-); when 5 < pH < 8, it mainly existed in the form of zwitterion ($OFX^\pm$). According to Fig. 5(b), the pH_{pzc} of FMBC was 6.76. Therefore, when pH < 6.76, electrostatic repulsion occurred between the positively charged surface of FMBC and OFX^+ in solution. Additionally, the presence of a large number of H^+ ions in the solution might compete with OFX for surface combining sites on the FMBC,[52] leading to a decrease in adsorption, a phenomenon that became more pronounced the lower the pH value. And with the gradual increase of pH, this electrostatic repulsive effect decreased. In the near-neutral range, groups such as –OH and –NH_2 in the OFX molecular structure could form hydrogen bonds with the oxygen-containing functional groups protonated on the FMBC surface to promote adsorption.[53] In addition, the OFX molecules that contained zwitterions had the lowest solubility and the highest hydrophobicity and that promoted the OFX molecules to fast reach FMBC surfaces,[54] which resulted in the highest OFX adsorption at pH 7 under hydrogen bonding and hydrophobic interactions. As the pH continued to increase from 7 to 12, the adsorption capacity of FMBC was significantly decreased due to the greater electrostatic repulsion between the negatively charged surface of FMBC and OFX^- and the large amount of OH^- in the solution prevented OFX from entering the FMBC surface.[55]

3.4.2 Effect of coexisting ions. The actual water body was diverse and complex, usually with multiple impurities coexisting. Therefore, the effect of coexisting ions on the adsorption of OFX on FMBC was investigated. To maximize the error reduction, the experiments were performed with cationic salt of chloride and anionic salt of sodium.

As shown in Fig. 6(a), in terms of coexisting anions, the addition of SO_4^{2-} had a small enhancement on the adsorption, which may be due to ionic hydrolysis reactions and the formation of a small amount of hydrogen bonds.[53,56] The addition of Cl^- had little effect on the adsorption capacity, and when the Cl^- concentration was 0.01 mol L^{-1}, it promoted the adsorption process, probably because the solubility of OFX was reduced by salting out, and therefore the adsorption capacity was enhanced.[56] However, the addition of NO_3^-, CO_3^{2-}, and PO_4^{3-} showed a significant decrease in the adsorption capacity. As the adsorbent preferred to adsorb the less hydrated anions, and the affinity of anions to adsorbent followed the order: $OH^- < PO_4^{3-} < CO_3^{2-} < NO_3^-$,[57] which explained why the inhibition of NO_3^- on OFX adsorption was the most. In terms of coexisting cations (Fig. 6(b)), the addition of Na^+ and K^+ had a small effect on the adsorption capacity, while the addition of Ca^{2+} and Mg^{2+} showed a significant decrease in adsorption with increasing concentration. This was because the priority of cations binding to organic matter usually was expressed as follows: alkaline-

Open Access Article. Published on 04 November 2022. Downloaded on 11/2/2025 4:32:41 PM.
This article is licensed under a Creative Commons Attribution-NonCommercial 3.0 Unported Licence.

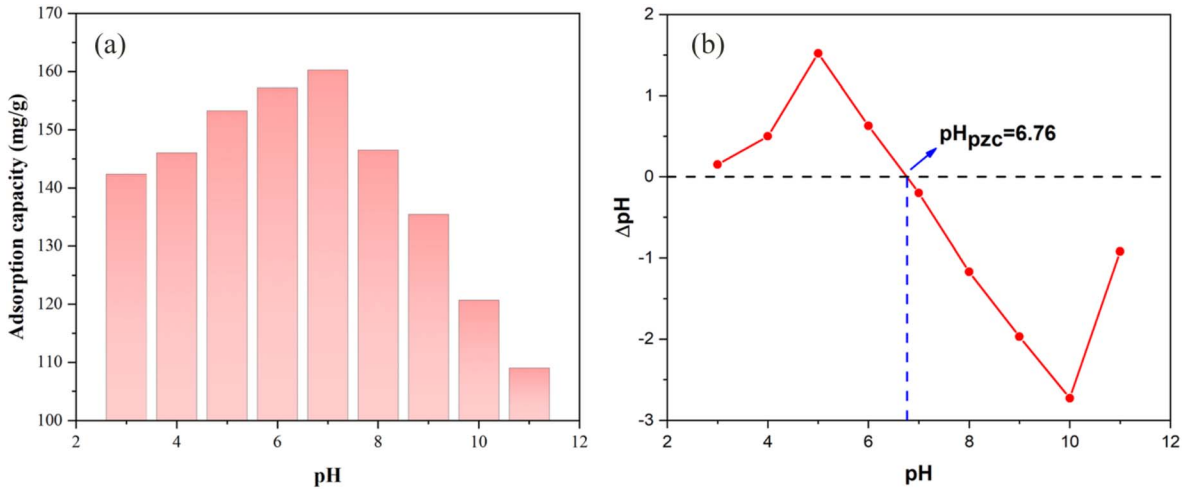

Fig. 5 (a) Effect of initial pH on the adsorption of OFX and (b) pH_{pzc} of FMBC.

earth metal cations (Ca^{2+} and Mg^{2+}) > alkali-metal cations (Na^{+} and K^{+}).[58] Therefore, during adsorption, Ca^{2+} and Mg^{2+} bounded more strongly to the adsorption sites. Besides, the hydrated radius of divalent Ca^{2+} was the largest,[48] and thus the inhibition was the most pronounced.

3.5 Adsorption mechanism

Fig. 7 showed that schematic diagram of the adsorption removal mechanism of OFX by FMBC. The discussion on the effect of initial solution pH showed that electrostatic interactions played an important role in the adsorption process.

The SEM and BET analyses revealed that after alkali modification and metal modification of FMBC, the specific surface area and total pore volume highly increased, resulting in a significant increase in OFX adsorption capacity. The average pore size and pore size distribution graphs indicated that FMBC was mainly mesoporous in structure, it could be speculated that this porosity structure of FMBC not only afforded more active sites for OFX but also made it easier for smaller OFX molecules to migrate into porous surroundings, causing a pore filling effect.

As shown in Fig. 8, the peaks observed at 3434/3426 cm^{-1}, 2923/2920/2857/2828 cm^{-1}, 1638/1635 cm^{-1}, 1403/1400 cm^{-1}, and 1084/1069 cm^{-1} were associated with the –OH, C–H, C=C, C=C–O, and C–O bond stretching vibration,[59–62] and obvious sharp peaks M–O at 590 cm^{-1} were caused by the stretching vibration of the Fe (Co)–O bond.[42] It was clear that some changes took place in the characteristic peaks of Fourier transform infrared spectroscopy (FTIR) of FMBC before and after OFX adsorption, a new peak was found at 1446 cm^{-1} corresponding to a lower intensity C–H bond stretching vibration, which could be attributed to the CH_2 group on OFX,[63] indicating that OFX was successfully adsorbed by FMBC. The positions of functional groups on FMBC all changed, and the intensity of the characteristic peaks were all weakened, it could be inferred that the corresponding functional groups were

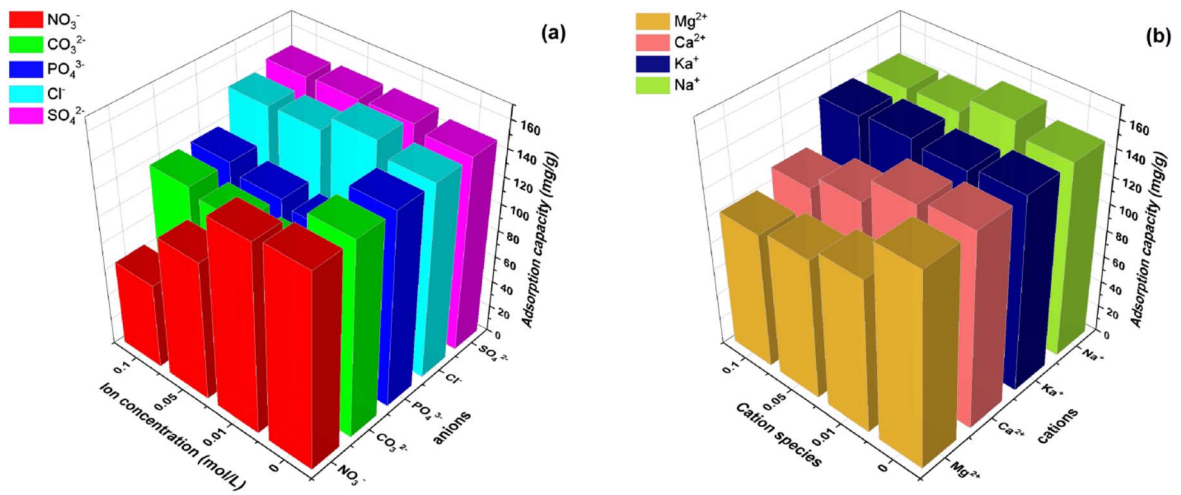

Fig. 6 Effect of (a) anions and (b) cations on the adsorption of OFX by FMBC.

 © 2022 The Author(s). Published by the Royal Society of Chemistry

Open Access Article. Published on 04 November 2022. Downloaded on 11/2/2025 4:32:41 PM.
This article is licensed under a Creative Commons Attribution-NonCommercial 3.0 Unported Licence.

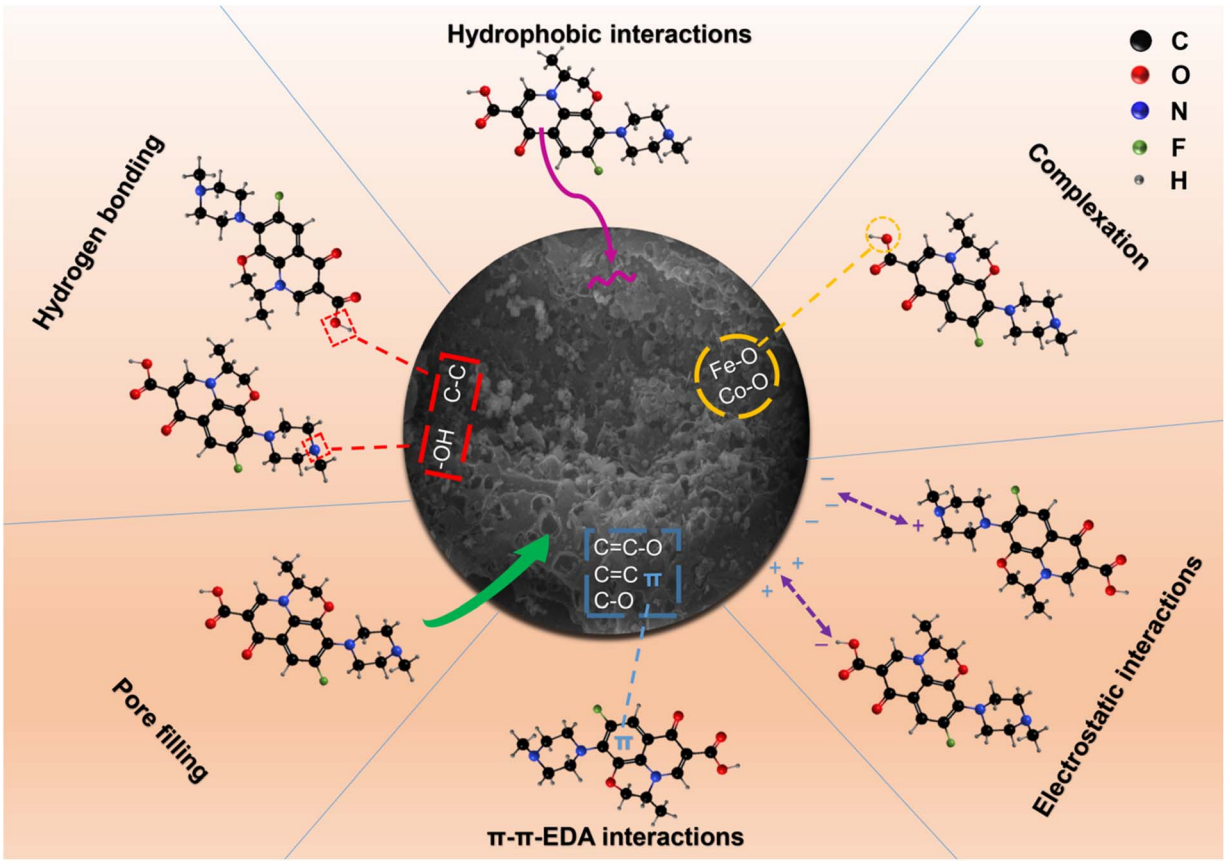

Fig. 7 Schematic diagram of the adsorption removal mechanism of OFX by FMBC.

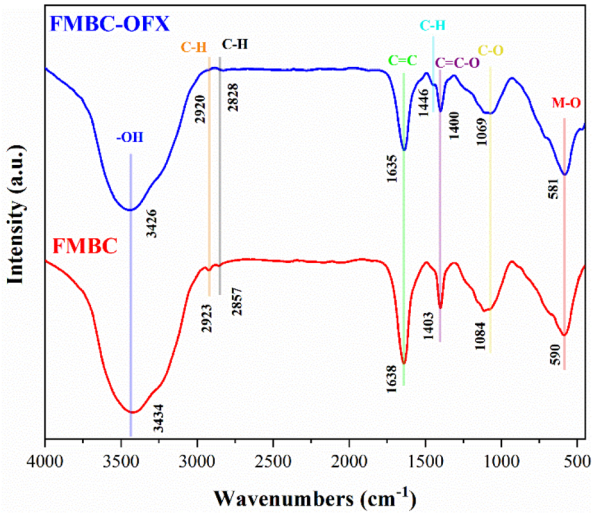

Fig. 8 FTIR spectra of FMBC before and after OFX adsorption.

involved in the adsorption reaction of OFX. The –OH and C–C bonds on FMBC could act as hydrogen bond donors and form hydrogen bonds with the hydrogen bond acceptors (–OH and $–NH_2$) on the OFX benzene ring. Studies confirmed that hydrogen bonds can promote the adsorption of polar organic compounds on biochar.[64] The OFX could serve as a π-electron acceptor due to the F group of the benzene ring's strong electron-withdrawing ability, and the C=C bond and oxygen-containing functional groups (C=C–O and C–O) on the surface of FMBC readily acted as a π-electron donor, thus forming π–π EDA interactions and enhancing the adsorption of OFX.[43] The peak position of M–O stretching vibrations was also shifted to some extent, indicating that Fe (Co)–O may provide more adsorption sites for OFX adsorption.

Fig. 9(a)–(d) showed the XPS patterns of C 1s, O 1s, Fe 2p, and Co 2p of FMBC before and after the adsorption of OFX. After adsorption of OFX, for C1s, the peak area ratio of C–C/C=C decreased from 66% to 57.09% for a significant decrease, the peak area ratio of O–C=O decreased from 8.46% to 7.86%, and the peak area ratio of C–O increased from 24.78% to 35.05% for a significant increase. Probably due to that they combined with the groups in OFX through hydrogen bonding and π–π EDA interactions,[65] which was consistent with the FTIR results. For O 1s, the peak area ratio of C=O increased from 29.97% to 31.66%, which might be a result of its serving as electron donors during OFX adsorption.[66] The peak area ratio of M–O in O 1s increased from 24.72% to 25.82%, and the peak intensities and binding energies of both Fe 2p and Co 2p also changed, indicating that Fe and Co may be engaged in the adsorption of OFX through surface complexation, which improved the adsorption capacity of FMBC.[67]

Open Access Article. Published on 04 November 2022. Downloaded on 11/2/2025 4:32:41 PM.
This article is licensed under a Creative Commons Attribution-NonCommercial 3.0 Unported Licence.

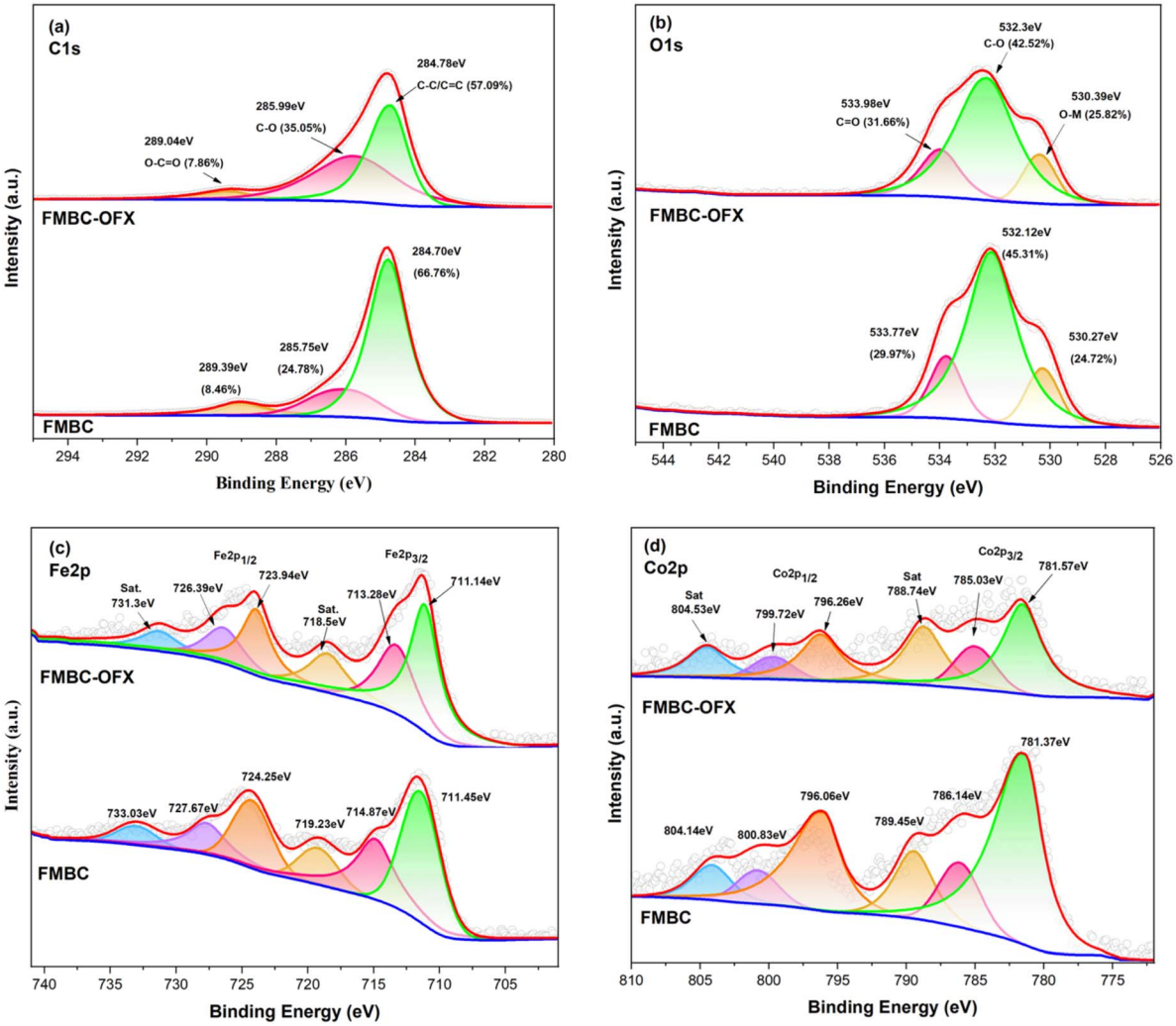

Fig. 9 (a–d) XPS spectra of FMBC before and after the adsorption of OFX by FMBC.

In summary, multiple adsorption mechanisms, among physical and chemical interactions, were involved in the adsorption of OFX by FMBC, including pore filling, electrostatic interactions, hydrogen bonding, hydrophobic interactions, complexation, and π–π EDA interactions.

3.6 Material stability and recycling

3.6.1 TG analysis. The thermogravimetric (TG) curves of CFB, BC, and FMBC were shown in Fig. 10(a), from which it could be observed that weight loss could be mainly divided into three stages. Stage I occurred between 25–125 °C, with weight losses of 13.18, 11.05, and 4.89% for CFB, BC, and FMBC, respectively, owing to the evaporation of moisture adsorbed on the outer surface of the materials.[68] Stage II occurred between 125–390 °C, with weight losses of 43.14, 8.04, and 3.44% for CFB, BC, and FMBC, respectively, for CFB it was mainly caused by the decomposition of cellulose and hemicellulose, the main components of its biomass.[37] While for BC and FMBC it was mainly due to the elimination of labile oxygen-containing functional groups.[32] Stage III occurred between 390–733 °C, with weight losses of 18.94, 4.83, and 12.36% for CFB, BC, and FMBC, respectively, for CFB it was mainly the thermal decomposition of residual cellulose and lignin,[69] BC was mainly due to the decomposition of the carbon skeleton. While FMBC had two distinct weight loss processes at this stage, between 661.84–709.39 °C could be attributed to the loss of more stable oxygen-containing functional groups,[32] and between 709.39–733 °C to the decomposition of the carbon skeleton. Continuously warmed up to 800 °C, their weight remained almost unchanged. Overall, CFB had the largest total weight loss of 75.26% and BC had a total weight loss of 23.92%, indicating that the conversion of biomass to biochar greatly reduced the weight loss of the material. The comparison between FMBC and BC showed that the weight of FMBC did not change much with the increase in temperature (25–661.84 °C), which proved its excellent thermal stability and high-temperature resistance, and the total weight loss rate was only 20.69%.

3.6.2 Leaching of Fe and Co. To avoid secondary pollution to the environment of FMBC, hence the metal of Fe and Co concentrations leaching from FMBC at different initial pH were

 © 2022 The Author(s). Published by the Royal Society of Chemistry

Open Access Article. Published on 04 November 2022. Downloaded on 11/2/2025 4:32:41 PM.
This article is licensed under a Creative Commons Attribution-NonCommercial 3.0 Unported Licence.

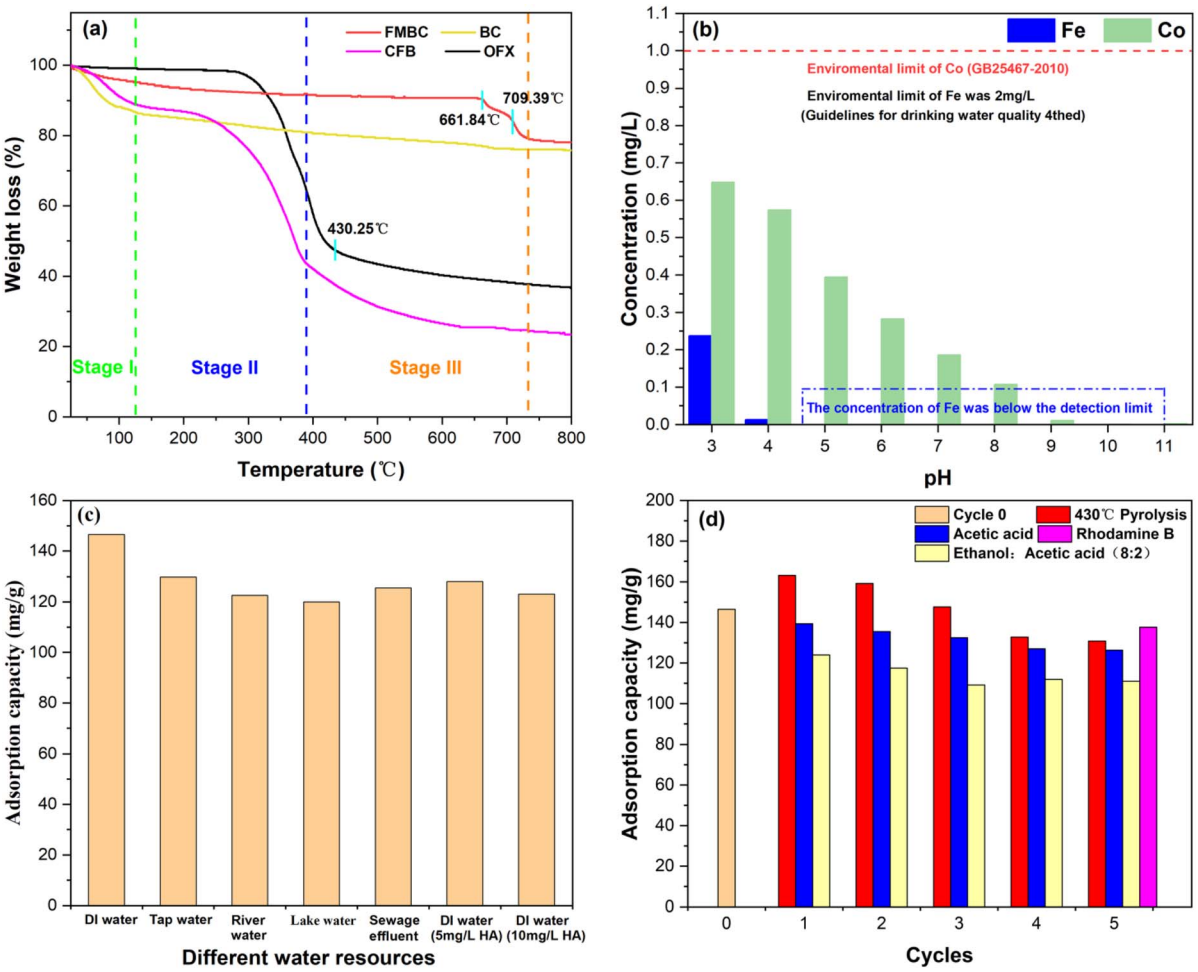

Fig. 10 (a) TG curves of OFX, CFB, BC, and FMBC; (b) leaching of Fe and Co in OFX solution at different initial pH; (c) effect of different water resources on OFX adsorption by FMBC; (d) adsorption capacity of FMBC in recycling experiment.

determined by inductively coupled plasma emission spectrometer (ICP). From the results in Fig. 10(b), it could be seen that the leaching concentration of Co decreased with the increase of solution pH in the range of pH 3 to 11, and the leaching concentration ranged from 0.001 to 0.648 mg L^{-1}. Nevertheless, the leaching concentration of Co did not exceed the limit value of Co (1 mg L^{-1}) in the pollutant emission standard (GB 25467-2010). Meanwhile, the leaching concentration of Fe was detected only in pH = 3 and pH = 4 as 0.237 mg L^{-1} and 0.013 mg L^{-1}, respectively, while the concentrations in other pH conditions were below the detection limit, and their detected concentrations were also much lower than the limit value of Fe (2 mg L^{-1}) in the WHO Guidelines for Drinking-water Quality (fourth edition). The above showed that the FMBC synthesized in this study had remarkable chemical stability and environmental safety.

Table 3 Comparison of the adsorption capacity of OFX using FMBC with other reported adsorbents

Adsorbents	Raw materials	q_e (mg g^{-1})
KMSBC[41]	Sludge	47.4
BTSCa[51]	Textile dyeing industrial sludge	21.6
rGO-MoS_2 heterostructure[73]	Graphite powder	37.3
AlS-KLB[74]	Kaolin	33.6
$LaFeO_3$/lignin-biochar[75]	Lignin	30.4
RHA[76]	Rice husk ash	6.3
FMBC (this study)	Cedar bark	142.2

3.6.3 Different water resources. Different water resources including water from river water, lake water, tap water, sewage effluent, and DI water with/without humic acid (HA) were collected and used to examine the adsorption capacity of OFX on FMBC. The results were shown in Fig. 10(c), and it could be seen that DI water had the highest adsorption capacity for OFX, which could reach 146.50 mg g^{-1}. The next highest adsorption capacity was in tap water (129.76 mg g^{-1}), which may be due to salting caused by the presence of large amounts of Cl^- during the disinfection process,[42] which was consistent with the above analysis of the effect of coexisting ions. And then the adsorption capacity was (with 5 mg L^{-1} HA) DI water (128.00 mg g^{-1}) > sewage effluent (125.57 mg g^{-1}) > (with 10 mg L^{-1} HA) DI water (123.02 mg g^{-1}) > river water (122.58 mg g^{-1}) > lake water

Open Access Article. Published on 04 November 2022. Downloaded on 11/2/2025 4:32:41 PM. This article is licensed under a Creative Commons Attribution-NonCommercial 3.0 Unported Licence.

(119.97 mg g^{-1}) in order. In summary, no matter what kind of water resources, the adsorption capacity of OFX on FMBC exceeded 119.97 mg g^{-1}, showing that the presence of natural matter in the water had little effect on the OFX adsorption process due to its unique physicochemical features.

3.6.4 Recycling experiment. Recycling and reusing were important indicators to evaluate the cost-effectiveness of adsorbents. Competitive adsorbents should exhibit a good reusable and recycling capability in industrial applications, which could substantially reduce the consumption and economic cost of biochar, while also reducing the dependence on continuous supply.

Thermal regeneration was an effective method to achieve desorption. From the above TG analysis, it could be seen that the temperature of thermal regeneration should not be higher than 661.84 °C to ensure that the internal structure of FMBC was not destroyed. From the TG curve of OFX in Fig. 10(a), OFX basically finished the pyrolysis at 430.25 °C, and the weight loss remained basically constant for the subsequent increase in temperature. Therefore, the temperature of thermal regeneration in the recycling experiment was determined to be 430 °C. Solvent regeneration was often used in chemical regeneration, according to the theory of similar mutual solubility, OFX was readily soluble in organic solvents because it was an organic compound.[70]

From the comparison of the three different desorption methods in Fig. 10(d), it could be shown that thermal desorption at 430 °C was the best. The adsorption capacity in the first three cycles was better than that before the cycle, and the highest adsorption capacity was 163.26 mg g^{-1}, which was 111.44% of the adsorption capacity before the cycle (146.50 mg g^{-1}). This could be that the calcination process promoted further formation of pores inside the FMBC, thus increasing the adsorption active sites. And it gradually decreased from the 4th cycle, which may be due to the disruption of the internal pore structure of FMBC caused by repeated pyrolysis and the occupancy or blockage of the pores by the residual ash from the decomposition of OFX.[44] Desorption by acetic acid was superior to the mixture (alcohol: acetic acid), probably due to the physical and chemical properties of OFX, which was soluble in acetic acid and able to desorb from FMBC into the acetic acid solution, and then gradually decreased adsorption may be due to the residual OFX on the surface of the biochar, thus occupying part of the active site and inhibiting the reactivation.[71] After five cycles, the three methods were still able to reach 89.31% (130.84 mg g^{-1}), 86.24% (126.34 mg g^{-1}) and 75.78% (111.02 mg g^{-1}) of the adsorption capacity before recycling, respectively. In addition, FMBC showed a high sorption capability of Rhodamine B (137.67 mg g^{-1}) even after 5 cycles in OFX removal, it was higher than the nanosorbent material prepared by Shaswat.[72] In a word, it showed that FMBC had high reusability and improved the utilization of biochar.

3.6.5 Magnetic properties of materials. Magnetic separation was a convenient and fast method to recycle adsorbed material. To verify the magnetic recovery performance of the material, the magnetic properties of FMBC before and after adsorption of OFX and FMBC-OFX (5 times desorption at 430 °C) were measured using vibrating-sample-magnetometry (VSM) at 25 °C over an applied magnetic field range of ±20 000 Oe, and the hysteresis loops were shown in Fig. S4.† The saturation magnetization (M_s) of FMBC, FMBC-OFX, and FMBC-OFX (5 times desorption at 430 °C) were 14.02, 10.00, and 10.98 emu g^{-1}, remnant magnetization (M_r) were 4.68, 2.55, and 4.85 emu g^{-1}, while coercive force (H_c) were 437.76, 218.88, and 802.55 Oe, respectively. Based on the high H_c of the three, it was shown that FMBC was a hard magnetic property and could maintain its magnetic properties for a long time after magnetization,[42] and this study showed that FMBC could maintain high magnetic properties after five times thermal regeneration. Fig. S5† exhibited the magnetic attraction effect of FMBC. The adsorbents were tightly adsorbed towards the bottle wall for 1 minute, verifying again that FMBC had excellent magnetism and could be easily separated, recovered, and reused from the aqueous solution.

3.7 Comparison with other adsorbents

The capacity of the adsorbent FMBC prepared towards the adsorption of OFX was compared with that of other adsorbents already reported in the literature and the data was shown in Table 3. The comparison of Table 3 showed that the adsorbent FMBC prepared in this study was superior to previous studies on the adsorption performance of OFX compared to those that had been reported on the adsorbent performance of OFX in recent years.

4. Conclusions

The residual antibiotics in water could cause potential harm to the environment and human beings, and it was of practical significance to find an efficient, green, and inexpensive adsorbent to remove the antibiotics from water. In this study, FMBC was effective in removing OFX from water. The BET showed that FMBC possessed a higher specific surface area, nearly 11 times higher than BC, and the pore structure was predominantly mesoporous. SEM-EDS observed the successful loading of Fe and Co on the biochar surface, and XRD further confirmed the presence of Fe and Co in the form of metal oxides and alloys. XPS and FTIR analyses showed that FMBC possessed abundant surface functional groups. The saturation adsorption capacity of FMBC (142.19 mg g^{-1}) was 10 times higher than that of BC (14.2864 mg g^{-1}). Pore filling, electrostatic interactions, hydrogen bonding, hydrophobic interactions, complexation, and π–π electron donor–acceptor interactions were possible mechanisms for OFX adsorption by FMBC. In different environmental conditions (coexisting ions, different water resources) and tests (TG, metal leaching, VSM), it showed good thermal stability, the leaching concentrations of both Fe and Co were well below the environmental limits, and the good magnetic properties made it easy to be separated from water. The FMBC was desorbed using thermal regeneration, acetic acid, and (alcohol : acetic acid) mixture, and after five cycles it still achieved a 75.78%–89.31% of adsorption capacity before recycling. Consequently, the FMBC synthesized in this study

 © 2022 The Author(s). Published by the Royal Society of Chemistry

Open Access Article. Published on 04 November 2022. Downloaded on 11/2/2025 4:32:41 PM.
This article is licensed under a Creative Commons Attribution-NonCommercial 3.0 Unported Licence.

was an efficient, inexpensive, environmentally safe, and reusable adsorbent with great potential for OFX removal application in actual water bodies.

Author contributions

Jiajie Hao: investigation, writing – original draft, writing – review & editing. Lieshan Wu: conceptualization, supervision. Xiaowei Lu: methodology. Yalin Zeng: data curation. Bing Jia: data curation. Tingting Luo: validation. Shixing He: visualization. Liuling Liang: resources.

Conflicts of interest

There are no conflicts to declare.

Acknowledgements

This work was financially supported by grant from Science and Technology Research and Development Program of Guangxi Zhuang Autonomous Region of China (no. AB21196039).

References

1 M. Malakootian, A. Nasiri and H. Mahdizadeh, *Water Sci. Technol.*, 2018, **78**, 2158–2170.
2 T. Nguyen, Q. Truong, C. Chen, R. Doong, W. Chen and C. Dong, *Bioresour. Technol.*, 2022, **346**, 126351.
3 C. Ratia, R. G. Soengas and S. M. Soto, *Front. Microbiol.*, 2022, **13**, 846959.
4 Y. Deng, A. Debognies, Q. Zhang, Z. Zhang, Z. Zhou, J. Zhang, L. Sun, T. Lu and H. Qian, *Aquat. Toxicol.*, 2022, **244**, 106084.
5 H. Zhang, Y. Jia, S. K. Khanal, H. Lu, H. Fang and Q. Zhao, *Environ. Sci. Technol.*, 2018, **52**, 6476–6486.
6 P. Kovalakova, L. Cizmas, T. J. McDonald, B. Marsalek, M. Feng and V. K. Sharma, *Chemosphere*, 2020, **251**, 126351.
7 G. Zhang, X. Liu, S. Lu, J. Zhang and W. Wang, *Chemosphere*, 2020, **242**, 125269.
8 Q. Dinh, E. Moreau-Guigon, P. Labadie, F. Alliot, M. Teil, M. Blanchard, J. Eurin and M. Chevreuil, *Sci. Total Environ.*, 2017, **575**, 758–766.
9 Y. Ma, P. Li, L. Yang, L. Wu, L. He, F. Gao, X. Qi and Z. Zhang, *Ecotoxicol. Environ. Saf.*, 2020, **196**, 110550.
10 R. Kaur, J. P. Kushwaha and N. Singh, *J. Electrochem. Soc.*, 2019, **166**, H250–H261.
11 R. Kaur, J. P. Kushwaha and N. Singh, *Sci. Total Environ.*, 2019, **677**, 84–97.
12 A. S. Maia, P. M. L. Castro and M. E. Tiritan, *J. Chromatogr. B: Anal. Technol. Biomed. Life Sci.*, 2016, **1029–1030**, 174–183.
13 L. Yan, Y. Liu, Y. Zhang, S. Liu, C. Wang, W. Chen, C. Liu, Z. Chen and Y. Zhang, *Bioresour. Technol.*, 2020, **297**, 122381.
14 A. Arabpour, S. Dan and H. Hashemipour, *Arab. J. Chem.*, 2021, **14**, 103003.
15 E. D. D. Freitas, H. J. D. Almeida and M. G. A. Vieira, *Appl. Clay Sci.*, 2017, **146**, 503–509.
16 V. K. Gupta, S. Agarwal, A. K. Bharti and H. Sadegh, *J. Mol. Liq.*, 2017, **230**, 667–673.
17 L. Li, D. Zou, Z. Xiao, X. Zeng, L. Zhang, L. Jiang, A. Wang, D. Ge, G. Zhang and F. Liu, *J. Clean. Prod.*, 2019, **210**, 1324–1342.
18 Z. Ren, B. Jia, G. Zhang, X. Fu, Z. Wang, P. Wang and L. Lv, *Chemosphere*, 2021, **262**, 127895.
19 K. N. Palansooriya, Y. S. Ok, Y. M. Awad, S. S. Lee, J. Sung, A. Koutsospyros and D. H. Moon, *J. Environ. Manage.*, 2019, **234**, 52–64.
20 J. Lehmann and S. Joseph, *Biochar for Environmental Management Science & Technology*, 2009, vol. 25, pp. 15801–15811.
21 C. E. R. Barquilha and M. C. B. Braga, *Bioresour. Technol. Rep.*, 2021, **15**, 100728.
22 N. Cheng, B. Wang, P. Wu, X. Lee, Y. Xing, M. Chen and B. Gao, *Environ. Pollut.*, 2021, **273**, 116448.
23 X. Zhu, C. Li, J. Li, B. Xie, J. Lü and Y. Li, *Bioresour. Technol.*, 2018, **263**, 475–482.
24 E. Butnaru, D. Pamfil, E. Stoleru and M. Brebu, *Biomass Bioenergy*, 2022, **159**, 106413.
25 J. O. Ighalo and A. G. Adeniyi, *Journal of Water Process Engineering*, 2020, **35**, 101228.
26 S. Liang, PhD thesis, Central South University, 2012.
27 S. Feng, S. Cheng, Z. Yuan, M. Leitch and C. C. Xu, *Renewable Sustainable Energy Rev.*, 2013, **26**, 560–578.
28 X. Zhang, Y. Li, M. Wu, Y. Pang, Z. Hao, M. Hu, R. Qiu and Z. Chen, *Bioresour. Technol.*, 2021, **320**, 124264.
29 J. Zhou, F. Ma and H. Guo, *Chem. Eng. J.*, 2020, **384**, 123290.
30 M. Thommes, K. Kaneko, A. V. Neimark, J. P. Olivier, F. Rodriguez-Reinoso, J. Rouquerol and K. S. W. Sing, *Pure Appl. Chem.*, 2015, **87**, 1051–1069.
31 Y. Sun, L. Zheng, X. Zheng, D. Xiao, Y. Yang, Z. Zhang, B. Ai and Z. Sheng, *Front. Chem.*, 2022, **9**.
32 X. Wang, Y. Lu, T. Zhu, S. Chang and W. Wang, *Chem. Eng. J.*, 2020, **388**, 124317.
33 Q. Ye, J. Wu, P. Wu, S. Rehman, Z. Ahmed and N. Zhu, *Chem. Eng. J.*, 2021, **417**, 129111.
34 X. Luo, H. Ma, H. Ren, X. Zou, Y. Wang, X. Li, Z. Shen, Y. Wang and L. Cui, *J. Colloid Interface Sci.*, 2021, **590**, 622–631.
35 A. Herath, C. A. Layne, F. Perez, E. B. Hassan, C. U. Pittman and T. E. Mlsna, *Chemosphere*, 2021, **269**, 128409.
36 Z. Zheng, B. Zhao, Y. Guo, Y. Guo, T. Pak and G. Li, *Sci. Total Environ.*, 2021, **787**, 147397.
37 S. Han and P. Xiao, *Sep. Purif. Technol.*, 2022, **287**, 120533.
38 Y. Wen, M. Liu, S. Li, L. Su, Y. Wang, Z. Zhou, N. Zhou and R. Li, *Chem. Eng. J.*, 2022, **446**, 137188.
39 J. Deng, Y. Zhou, Y. Zhao, L. Meng, T. Qin, X. Chen, K. Li and S. Yuan, *Energy*, 2022, **244**, 122602.
40 Z. Wang and H. M. Jang, *Bioresour. Technol.*, 2022, **351**, 127025.
41 Y. Ma, T. Lu, L. Yang, L. Wu, P. Li, J. Tang, Y. Chen, F. Gao, S. Cui, X. Qi and Z. Zhang, *Environ. Pollut.*, 2022, **298**, 118833.
42 J. Zhang, W. Lu, S. Zhan, J. Qiu, X. Wang, Z. Wu, H. Li, Z. Qiu and H. Peng, *Sep. Purif. Technol.*, 2021, **276**, 119296.
43 X. Geng, S. Lv, J. Yang, S. Cui and Z. Zhao, *J. Environ. Manage.*, 2021, **280**, 111749.

Open Access Article. Published on 04 November 2022. Downloaded on 11/2/2025 4:32:41 PM.
This article is licensed under a Creative Commons Attribution-NonCommercial 3.0 Unported Licence.

44 S. Zeng, Y. Choi and E. Kan, *Sci. Total Environ.*, 2021, **750**, 141691.
45 A. Nasiri, S. Rajabi, M. Hashemi and H. Nasab, *Sep. Purif. Technol.*, 2022, **296**, 121366.
46 Z. Liu, X. Fang, L. Chen, B. Tang, F. Song and W. Li, *Sustainability*, 2022, **14**, 5892.
47 W. A. Shaikh, R. U. Islam and S. Chakraborty, *J. Environ. Chem. Eng.*, 2021, **9**, 104982.
48 T. Nguyen, Q. Truong, C. Chen, W. Chen and C. Dong, *Bioresour. Technol.*, 2022, **351**, 127043.
49 J. Song, S. A. Messele, L. Meng, Z. Huang and M. Gamal El-Din, *Water Res.*, 2021, **194**, 116930.
50 Y. Zhou, X. Hu, Y. Zhang, X. Chen, H. Zhao, Q. Fu, F. Xu and Y. Gao, *Appl. Surf. Sci.*, 2021, **566**, 150657.
51 V. Singh and V. C. Srivastava, *Biomass Conversion and Biorefinery*, 2022.
52 Y. Zhou, S. Cao, C. Xi, X. Li, L. Zhang, G. Wang and Z. Chen, *Bioresour. Technol.*, 2019, **292**, 121951.
53 S. He, Q. Chen, G. Chen, G. Shi, C. Ruan, M. Feng, Y. Ma, X. Jin, X. Liu, C. Du, C. He, H. Dai and C. Cao, *Microporous Mesoporous Mater.*, 2022, **335**, 111848.
54 H. M. Hamadeen and E. A. Elkhatib, *Environ. Res.*, 2022, **210**, 112929.
55 Z. Wen, J. Xi, J. Lu, Y. Zhang, G. Cheng, Y. Zhang and R. Chen, *J. Hazard. Mater.*, 2021, **411**, 124909.
56 Y. Zhang, C. Zhu, F. Liu, Y. Yuan, H. Wu and A. Li, *Sci. Total Environ.*, 2019, **646**, 265–279.
57 K. N. Palansooriya, S. Kim, A. D. Igalavithana, Y. Hashimoto, Y. Choi, R. Mukhopadhyay, B. Sarkar and Y. S. Ok, *J. Hazard. Mater.*, 2021, **415**, 125464.
58 S. Yang, P. Zong, X. Ren, Q. Wang and X. Wang, *ACS Appl. Mater. Interfaces*, 2012, **4**, 6891–6900.
59 G. Chen, H. Wang, L. Han, N. Yang, B. Hu, M. Qiu and X. Zhong, *J. Mol. Liq.*, 2021, **327**, 114807.
60 J. Dobrzyńska, A. Wysokińska and R. Olchowski, *J. Environ. Manage.*, 2022, **316**, 115260.
61 G. Kaur, N. Singh and A. Rajor, *Environ. Technol. Innovation*, 2022, **25**, 102176.
62 X. Zhou, L. Shi, T. B. Moghaddam, M. Chen, S. Wu and X. Yuan, *J. Hazard. Mater.*, 2022, **425**, 128003.
63 X. Wang, Z. Meng, X. Liu, T. Wang, X. Hu and X. Sun, *Environ. Sci.*, 2021, **42**, 2334–2342.
64 R. R. Solis, O. Dinc, G. Fang, M. N. Nadagouda and D. D. Dionysiou, *Environ. Sci.: Nano*, 2021, **8**, 960–977.
65 C. Xu, X. Tan, J. Zhao, J. Cao, M. Ren, Y. Xiao and A. Lin, *J. Hazard. Mater.*, 2021, **416**, 125785.
66 J. Wu, T. Wang, Y. Zhang and W. Pan, *Bioresour. Technol.*, 2019, **291**, 121859.
67 P. Wang, D. Zhang, H. Tang, H. Li and B. Pan, *J. Hazard. Mater.*, 2019, **371**, 513–520.
68 M. Zahoor, M. Wahab, S. M. Salman, A. Sohail, E. A. Ali and R. Ullah, *Bioinorg. Chem. Appl.*, 2022, **2022**, 1–17.
69 S. F. Lütke, A. V. Igansi, L. Pegoraro, G. L. Dotto, L. A. A. Pinto and T. R. S. Cadaval, *J. Environ. Chem. Eng.*, 2019, **7**, 103396.
70 R. Li, Y. Zhang, W. Chu, Z. Chen and J. Wang, *RSC Adv.*, 2018, **8**, 13546–13555.
71 A. Nasiri, M. Malakootian, M. R. Heidari and S. N. Asadzadeh, *J. Polym. Environ.*, 2021, **29**, 2660–2675.
72 S. V. Gupta and M. Ahmaruzzaman, *Int. J. Environ. Anal. Chem.*, 2022, 1–20.
73 A. Jaswal, M. Kaur, S. Singh, S. K. Kansal, A. Umar, C. S. Garoufalis and S. Baskoutas, *J. Hazard. Mater.*, 2021, **417**, 125982.
74 Y. Yang, Z. Zhong, J. Li, H. Du and Z. Li, *J. Hazard. Mater.*, 2022, **430**, 128500.
75 X. Chen, M. Zhang, H. Qin, J. Zhou, Q. Shen, K. Wang, W. Chen, M. Liu and N. Li, *Sep. Purif. Technol.*, 2022, **280**, 119751.
76 G. Kaur, N. Singh and A. Rajor, *J. Contam. Hydrol.*, 2021, **236**, 103737.

 © 2022 The Author(s). Published by the Royal Society of Chemistry